

# Sustainable Ketjenblack-Based Carbon Ink for 3D Extrusion Micro-Printing to Fabricate Flexible Supercapacitors

Christin Gellrich,<sup>[a]</sup> Yannik Bräuniger,<sup>[a]</sup> Ralf Schmidt,<sup>[b]</sup> Julia Grothe,<sup>[a]</sup> and Stefan Kaskel<sup>\*[a, b]</sup>

3D printing has attracted much attention in industry and academia because it offers simple, low-cost, versatile and environmentally-friendly manufacturing technologies and has been utilized to fabricate flexible electronics like supercapacitors, batteries and sensors. Finding a suitable printable ink is the most challenging task for 3D printing. Carbon materials have been widely used in 3D printing of flexible electronics due to their high electrical conductivity, chemical stability, non-toxicity, and high surface area with versatile pore structure. However, mostly toxic solvents like NMP and DMF as well as non-biodegradable polymer binders such as PVDF and PTFE

were used to fabricate printable inks. Herein, a sustainable carbon ink highly suitable for 3D extrusion printing for well-defined, flexible in-plane all-solid-state micro-supercapacitors (MSC) using only non-toxic and biodegradable ingredients is presented. The MSCs show high areal capacitances of up to  $13.41 \text{ mFCm}^{-2}$  and  $35.10 \text{ Fcm}^{-3}$  for  $5 \text{ mVs}^{-1}$  as well as excellent cycle stability even when mechanically stressed. Various suspension additives are explored for tuning the rheological behavior, conductivity, and electrochemical performance of MSCs.

## Introduction

The increasing demand for portable and flexible electronics, such as wearable and implantable biodiagnostics or heart sensors, reinforces the urge to develop lightweight and flexible energy storage systems that can reliably power such devices even when bended or folded.<sup>[1,2]</sup> In contrast to applications where high power and energy densities are the key requirements for the power source (e.g., for the usage in cars), properties like long lifetime for maintenance-free operation, flexibility and biocompatibility as well as effective miniaturization of all device components are crucial when it comes to biomedical applications *in-vivo*.<sup>[2,3]</sup> Here, especially micro-sensors for the continuous measurement and control of vital parameters in the human body or devices for the targeted provision of active substances are addressed.<sup>[2,4]</sup> But also for *ex-vivo* applications, small, thin and flexible energy storage devices are necessary to ensure excellent wearing comfort on skin or clothing.<sup>[2,5]</sup>

Micro-supercapacitors (MSC) are promising candidates as energy storage devices for those biotechnological applications.

They provide fast charging-discharging rates and extraordinary long cycle lifetime (up to millions of cycles) at high power densities.<sup>[6]</sup> Carbon materials are widely used as electrodes in MSCs because they usually exhibit a high surface-area, stability and conductivity; they are commercially available, non-toxic, cheap and biocompatible.<sup>[7,8]</sup> Especially MSCs with an in-plane, interdigitated configuration are attracting attention for powering flexible devices because they can be easily integrated on chips and flexible substrates. Furthermore, due to low electrode finger distances in the interdigital electrode architectures the ion transport resistance can be decreased and the ion accessibility improved resulting in an increased rate performance and decreased equivalent series resistance (ESR). Also in this design no separator needs to be used.<sup>[1,9]</sup>

To fabricate flexible, interdigital in-plane MSCs, extrusion 3D-printing, also known as direct ink writing (DIW), is a promising manufacturing method because a broad variety of materials such as metals and metal alloys,<sup>[10,11]</sup> polymers<sup>[12,13]</sup> and carbon suspensions<sup>[14,15]</sup> can be printed easily and quickly on different substrate materials. Especially in contrast to other microfabrication methods like photolithography and laser scribing, complicated, expensive, and toxic processing steps generating a large amount of material waste are avoided making the extrusion 3D printing one of the most economic fabrication methods. The raw material can be used efficiently, usually without post-processing or material removal.<sup>[16–18]</sup> The design and geometry of the printed structure can be freely selected and varied which is especially advantageous when fabricating complex geometries with asymmetric configuration and different materials.<sup>[1,16,19,20]</sup> During the extrusion process the ink or paste is continuously extruded layer-by-layer through a nozzle and the deposited material is then solidified, usually by applying heat or UV-light on a substrate to form well-defined objects.<sup>[21,22]</sup> The movement of the tip is controlled by a software containing 3D model data. The pressure inside the tip,

[a] C. Gellrich, Y. Bräuniger, Dr. J. Grothe, Prof. S. Kaskel

Department of Inorganic Chemistry I  
Technische Universität Dresden  
Bergstraße 66, 01069 Dresden (Germany)  
E-mail: stefan.kaskel@tu-dresden.de  
Homepage: <https://tu-dresden.de/mn/chemie/ac/ac1>

[b] R. Schmidt, Prof. S. Kaskel

Fraunhofer Institute for Material and Beam Technology (IWS)  
Winterbergstraße 28, 01277, Dresden (Germany)

 Supporting information for this article is available on the WWW under <https://doi.org/10.1002/batt.202300469>

 © 2023 The Authors. *Batteries & Supercaps* published by Wiley-VCH GmbH. This is an open access article under the terms of the Creative Commons Attribution License, which permits use, distribution and reproduction in any medium, provided the original work is properly cited.

which is necessary for the extrusion, can be controlled mechanically or pneumatically. In order to generate a constant volume flow, the pressure must be adjusted to the viscosity of the ink and the hydraulic resistance of the tip.<sup>[21]</sup> The extrusion 3D printing has been successfully used to fabricate micro-electrodes, e.g., in sensors,<sup>[23]</sup> supercapacitors<sup>[14,24]</sup> and microbatteries.<sup>[25]</sup>

Choosing a suitable electrode ink with the desired mechanical and chemical properties is the most crucial factor to successfully printing microelectronic components with high stability and resolution.<sup>[26]</sup> For the extrusion 3D printing in particular, the ink should have a relatively high viscosity (5–500.000 mPa s) and exhibit a shear thinning or pseudoplastic behavior meaning the viscosity of the fluid decreases when increasing the shear stress. This behavior enables the ink to flow through the tip as well as to cure fast afterwards, and thus a high resolution and stability of the resulting printed structure is achieved. Next to suitable physical properties (viscosity, surface tension and drying rate), the electrode ink should fulfill other important requirements like high conductivity, high ink stability with limited aggregation of the dispersed particles and good adhesion on the substrate. Furthermore, the ink should lead to printed electrodes with high power and energy densities as well as high mechanical and long-term stability.<sup>[18,26–28]</sup>

In recent years, especially graphene and graphene-oxide (GO) based inks have been extensively investigated and reported for printing electronics, because of their high theoretical surface area ( $2630 \text{ m}^2 \text{ g}^{-1}$ ), excellent conductivity and mechanical properties.<sup>[15,29–31]</sup> However, the fabrication of graphene-based inks exhibit several disadvantages. Usually, time consuming and expensive exfoliation steps using large amounts of toxic organic solvents such as dimethylformamide (DMF) and *N*-methyl-2-pyrolidone (NMP) are required. The high boiling points of NMP or DMF ( $> 150^\circ\text{C}$ ) are additionally preventing the use of heat-sensitive polymer substrates. Furthermore, the

fabrication of defect-free graphene involves additional post-processing steps (high temperature annealing, reduction of GO to graphene) often accompanied by the usage of strong and toxic reductive agents like hydrazine are further shortcomings hindering the extended application in industry.<sup>[18,32]</sup> In contrast to graphene, activated carbon (AC) is a widely available and low-cost material used in most commercially available supercapacitors. Additionally, AC possesses, next to a high specific surface area, a hierarchically pore structure with a wide pore size distribution containing micro- and mesopores.<sup>[1]</sup> Activated carbon has been already used to fabricate microelectronic devices. For example, Santhiago et al. could fabricate sensors on paper using carbon black-based ink in a laser printer, achieving a resolution of about 500  $\mu\text{m}$ .<sup>[33]</sup> Pech et al. used the inkjet printing technique to print MSCs using an ink with carbon black, polytetrafluoropropylene (PTFE) as polymer binder, Triton X100 as surfactant and ethylene glycol as solvent.<sup>[34]</sup> However, especially in the extrusion printing field ACs are mainly used in the form of composites as conductive agent for example in carbon black-polymer-composites.<sup>[35–39]</sup>

Herein, we present a low-cost, non-toxic, ecofriendly, and biodegradable activated carbon-based ink, highly suitable for extrusion 3D printing to fabricate flexible MSCs with high energy and power densities as well as excellent cycle lifetime, even when bended. First, we developed an ink formulation based on a suitable carbon mixture Ketjenblack and multiwalled carbon nanotubes (MWCNTs), ethylcellulose (EC) as a binder and cellulose-derived dihydrolevoglucosenone (cyrene) as solvent (Figure 1). Second, the optimized ink was applied to the extrusion printing process fabricating an in-plane, interdigital electrode structure using a polyaniline-based material (Kapton®) as flexible substrate material. Third, the printed structures were further processed to MSCs using a silver paste for contacting the device, Kapton foil as electrolyte confinement and different electrolytes (polyvinyl alcohol and sulfuric acid based ionogel (PVA/H<sub>2</sub>SO<sub>4</sub>), 0.1 M and 1 M sulfuric acid).

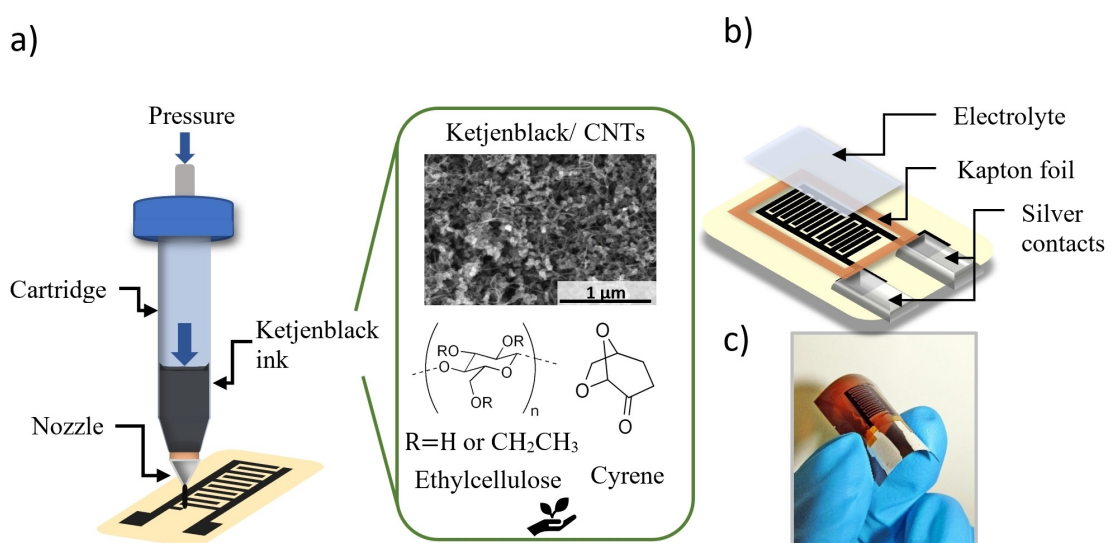


**Figure 1.** Schematic procedure of a) 3D extrusion printing the Ketjenblack/CNT based carbon ink with ethylcellulose as binder and cyrene as solvent, b) processing of the printed carbon structures to flexible, in-plane interdigital MSCs, c) picture of the final flexible MSC.

## Results and Discussion

### Characterization of the used AC material (Ketjenblack)

As primary carbon black material in the ink we used commercially-available Ketjenblack. This AC material is known for its high electrical conductivity, high surface area as well as open porous structure and is therefore considered to be superior to other carbon blacks.<sup>[40]</sup> Nitrogen physisorption measurements at  $-196^{\circ}\text{C}$  reveal that the used Ketjenblack material shows indeed a high surface area of  $1360 \text{ m}^2\text{g}^{-1}$  and a total pore volume of  $2.5 \text{ cm}^3\text{g}^{-1}$  (Figure S1a). The system exhibits a type IV isotherm, characteristic for a mesoporous pore structure. Besides mesopores mainly in the range of 2–5 nm also a considerable amount of micropores (12 % of the total pore volume) are dominating the pore structure (Figure S1b). Raman spectra reveal the D-band at  $1326 \text{ cm}^{-1}$  caused by the disordered carbon structures and also the G-band at  $1590 \text{ cm}^{-1}$  assigned to the graphitic carbon (Figure S1c). In addition, also the 2D ( $2636 \text{ cm}^{-1}$ ) as well as the D+G combination mode ( $2910 \text{ cm}^{-1}$ ) are observed which is typical for layered graphitic carbon.<sup>[41]</sup> The graphitic domains responsible for the high conductivity of the carbon material are also visible in TEM images (Figure S1d–e). The average particle size of the AC powder is mainly in the range of 20–50 nm and therefore in comparison to other carbon blacks very small. A small carbon particle size is in general advantageous in a printable ink formulation especially when small nozzle diameters are used. Additionally, it can be seen that the primary particles are interconnected forming a secondary network (Figure S1e). The graphitic domains with graphitic layers (distance:  $3.45 \text{ \AA}$ ) can be clearly seen in HRTEM image (Figure S1f).

### Optimization of the binder concentration

In this work, ethylcellulose (EC) is used as a polymeric binder. In comparison to other popular used binder materials like polyvinylidenefluoride (PVDF) or polytetrafluoroethylene (PTFE), EC is a biodegradable and more environmentally-friendly binder. Together with the solvent the binder plays a crucial role in the overall printability of the ink, because it determines the viscosity and rheological behavior of the ink by controlling the dispersion stability, wettability and uniform distribution of the particles. However, it is crucial to adjust a right binder concentration since a high binder content decreases the conductivity and overall electrochemical performance of the printed structure because it impedes the inter-particle connection as well as decreases the active surface area of the whole material, leading to lower capacitances. On the other hand a low binder content could lead to a diminished mechanical stability, cracks and unsuitable printing properties.<sup>[18,26,42]</sup>

To investigate the influence of the binder content and post annealing temperature on the specific resistance, AC based carbon thin films were prepared by spin coating the suspension

with binder content varied from 0.95 wt.% to 2.50 wt.% EC on activated glass substrates (Figure 2a). As expected, the specific resistance in general increases with increasing binder content. However, the carbon thin film with 1.69 wt.% exhibits an unexpected high sheet resistance indicating an unfavorable AC to binder ratio. AFM measurements of the thin films reveal that the surface morphology of the film with 1.69 wt.% EC is very inhomogeneous with particle agglomerates leading to a disturbed electron pathway and therefore high sheet resistances. By further increasing the EC-content (2.50 wt.%), these inhomogeneities could be prevented resulting in a homogeneous sheet morphology (Figures 2b and S2). Furthermore, it can be observed that the specific sheet resistance slightly decreases with increasing post-annealing temperature from room temperature to  $300^{\circ}\text{C}$ . This is mainly attributed to the complete evaporation of the solvent and the beginning decomposition of the binder at  $300^{\circ}\text{C}$ , as thermogravimetric (TG) analysis shows (Figure 2c). In order to avoid a complete decomposition of the binder (at around  $400^{\circ}\text{C}$ ) and to enable the use of polymer substrates, the temperature was not increased further and  $300^{\circ}\text{C}$  as post annealing temperature was chosen for all further investigations. The sheet resistances that could be obtained using Ketjenblack as active carbon material are in the range of 1.9–4.6  $\text{m}\Omega\text{m}$  and therefore very low in comparison to specific sheet resistances of similar binder-based suspensions (over  $1800 \text{ m}\Omega\text{m}$  for a graphene-EC-based suspension).<sup>[23]</sup>

In the next step, the carbon suspensions were used to fabricate thin film EDLCs (PVA/ $\text{H}_2\text{SO}_4$  as electrolyte) as well as used for printing interdigital MSC structures consisting of two symmetrical electrodes with 8 fingers each (Figure 3a) to evaluate the electrochemical performances using cyclic voltammetry (CV) and electrochemical impedance spectroscopy (EIS).

The EDLCs show the desired rectangular shape in the CV curve as expected for a pure capacitive energy storage behavior. The areal capacitances of the thin film EDLCs decreased with increasing binder content due to lower specific surface area of the carbon suspension (Figure 2d and e). The highest capacitance could be therefore achieved for the 0.95 wt.% EC content with  $12.66 \text{ mFcm}^{-2}$  for  $5 \text{ mVs}^{-1}$ ;  $7.87 \text{ mFcm}^{-2}$  for  $100 \text{ mVs}^{-1}$ . Further decreasing the EC content however led to severe cracks in the carbon matrix when drop casted on the electrode current collector. In general, it could be observed that with decreasing the binder content of the suspension, the probability of cracks and failures drastically increased especially when the material loading (volume of drop casted carbon suspension) was high. This was also visible for the printed MSCs (Figure 2f–i). If the binder content was too low (< 1.69 wt.% EC) the structures exhibit severe cracks and diminished substrate adhesion after solvent evaporation leading to a low mechanical stability. By further increasing the binder content, the crack formation could be inhibited and homogeneous structures were obtained. Furthermore, due to a higher viscosity of the suspension with a high EC content, thinner lines could be printed (0.95 wt.%  $450 \mu\text{m}$ , 2.50 wt.%  $350 \mu\text{m}$  line width) leading to a higher printable structure resolution.

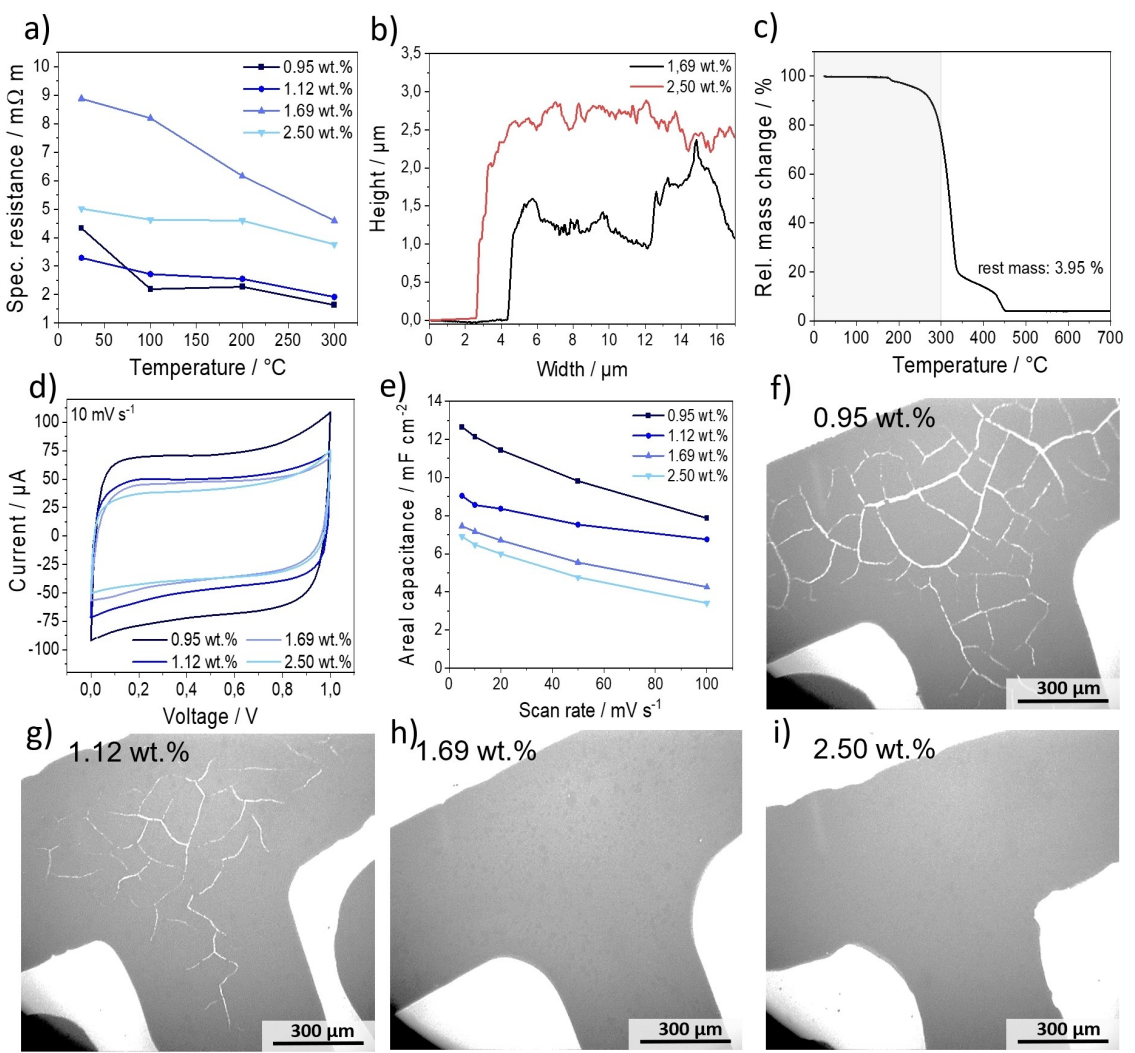


**Figure 2.** a) Specific resistance of the carbon sheets with different EC content and annealing temperatures, b) AFM profile of the carbon sheets with 1.69 wt.% and 2.50 wt.% EC content, c) TG analysis of the AC-4 powder under Argon atmosphere, d) CV curve and e) areal capacitances of the thin-film EDLCs with different EC-content, f–i) microscopic images of the printed structures with different EC-content.

The above-mentioned influences of the binder content are also reflected in the electrochemical performance of the printed MSCs. Although the specific surface area of the suspension with the highest EC content is the lowest, the MSCs showed the highest areal capacitance ( $8.61 \text{ mF cm}^{-2}$  at  $5 \text{ mVs}^{-1}$ ), probably due to a higher mechanical stability and crack free structure. Due to the discussed observations a binder content of 2.5 wt.% was chosen for all further investigations. However, for higher scan rates the areal capacitance significantly drops by 85 % for all analyzed suspensions to about  $1.5 \text{ mF cm}^{-2}$  at  $100 \text{ mVs}^{-1}$  (Figure 3b-d).

Impedance measurements conducted before cycling, after 10 cycles at  $10 \text{ mVs}^{-1}$  and after the whole measurement experiment (cycling from  $5\text{--}100 \text{ mVs}^{-1}$ , 5 cycles each scan rate) show that the equivalent serial resistance (ESR) drastically increases especially during the first 10 cycles from  $2.5 \text{ k}\Omega$  to  $10\text{--}15 \text{ k}\Omega$  probably mainly caused by the increasing electrode resistance due to failures and cracks in the electrode matrix during cycling

(Figure 3e). This indicates stability problems in the electrode material probably due to the detachment of the fine AC particles during swelling effects caused by the entrance of the electrolyte in the pore system leading to a lack of interparticle connection. The  $45^\circ$  rise of the impedance curve over a wide resistance range for all impedance measurements indicate a major ion diffusion problem inside the MSC system which is also visible in the CV curve at high scan rates.

#### Optimization of the electrode stability and conductivity with addition of CNTs

To increase the electrode stability, a further drastic increase of the binder content would be necessary leading to lower specific capacitances and conductivity of the electrode material. CNTs are known to possess an outstanding conductivity (usually between  $10^4$  to  $10^5 \text{ S cm}^{-1}$ ) and a high mechanical stability due

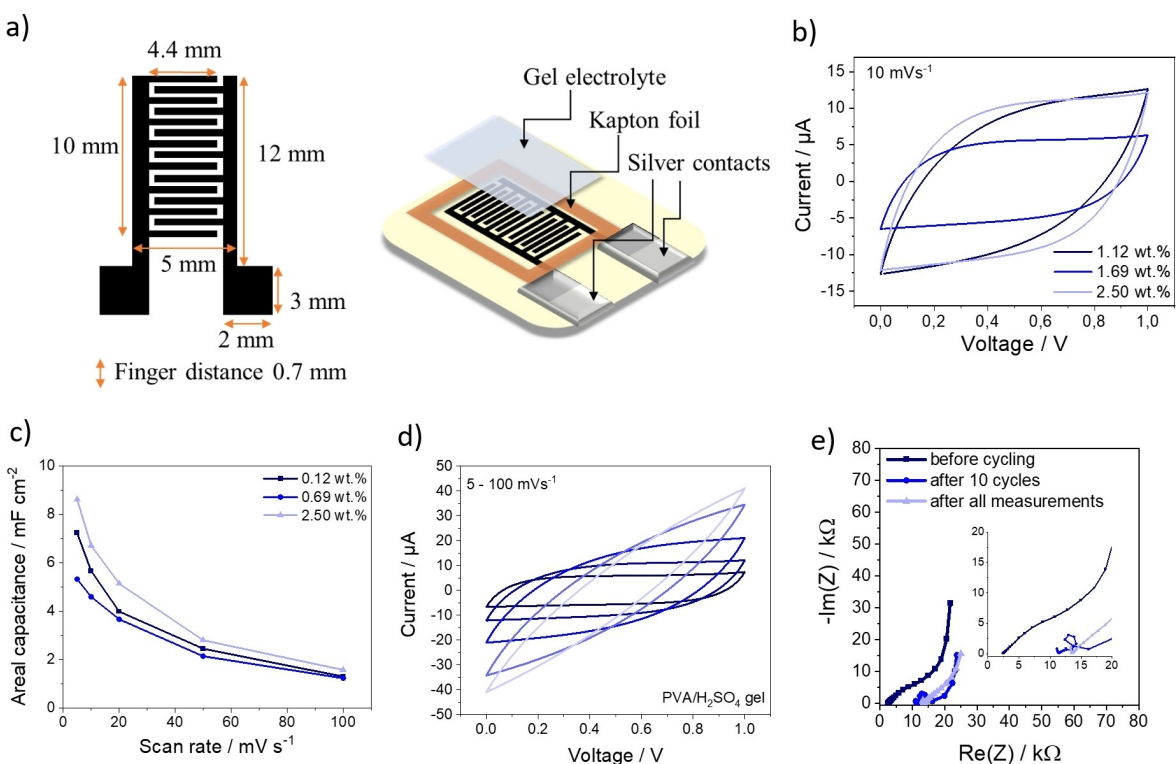


**Figure 3.** a) Extrusion 3D printed standard structure and post processing steps to MSC, b) and c) CV curves and capacitances of the MSCs with different EC content, d) and e) CV curve and impedance measurements of the MSC with 2.5 wt.% EC content.

to their high elasticity which allows them to adapt well to the volume changes of the electrodes during the loading and unloading processes.<sup>[7]</sup> However, especially in contrast to activated carbons like Ketjenblack, CNTs usually possess lower specific surface areas, which can lead to a decrease in the overall capacitance of the system. CNTs with a surface area of  $259 \text{ m}^2 \text{ g}^{-1}$  (Figure S3) were added to the AC mixture.

To ensure a high electrode stability and conductivity while still reaching high specific capacitances, different amounts of CNTs were added and the resulting rheological behavior, conductivity, printability, and electrochemical performance of the MSCs was evaluated.

First, the viscosity of the synthesized inks with different CNT content was measured at room temperature (Figure 4a). All suspensions show shear thinning, thixotropic behavior highly desirable for many printing techniques like 3D extrusion printing. They exhibit a viscosity of  $2\text{--}15 \text{ Pas}$  at a shear rate of  $1 \text{ s}^{-1}$  which is less than those of traditional filamentary printing ( $10^3\text{--}10^4 \text{ Pas}$  at  $1 \text{ s}^{-1}$ ) but much higher than ink used for inkjet printing ( $10^{-3} \text{ Pas}$  at  $1 \text{ s}^{-1}$ ) and similar to comparable inks for MSC extrusion printing.<sup>[14,23,25,43]</sup> However, the suspensions with high CNT content (CNT20d and CNT50d) needed to be diluted (notation "d" for a dilution) to decrease their high viscosity and ensure a suitable printability. Despite this dilution, a slight

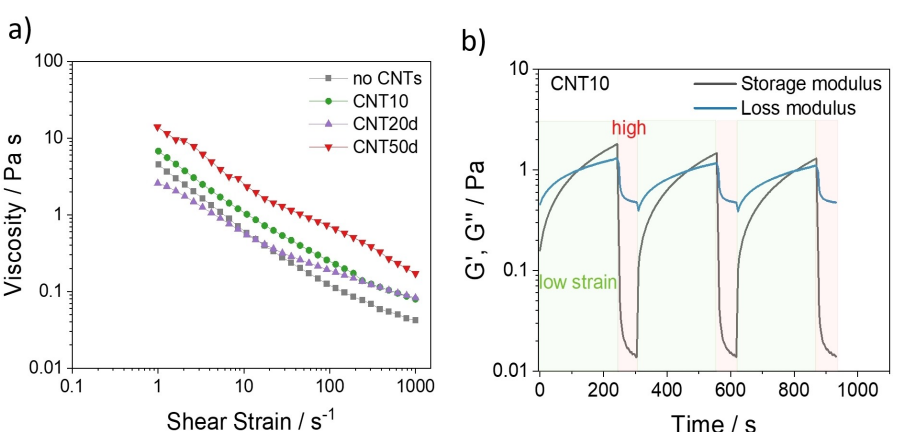


**Figure 4.** Rheological analysis of suspensions with different CNT amount. a) Viscosity as a function of shear rate and b) storage ( $G'$ ) and loss ( $G''$ ) modulus.

increase in viscosity with higher CNT content is still visible. Furthermore, rheological analysis with different strain (10 Pa (high strain for 60 s), 0.2 Pa (low strain for 250 s)) over several cycles were conducted. In Figure 4(b), three cycles for CNT10 are exemplarily shown. When strain is applied to the suspension,  $G'$  (storage modulus) and  $G''$  (loss modulus) rapidly decrease but return to their initial values after removing the load. Similar observations could be also made for the other analyzed AC–CNT suspensions (Figure S4). These results underline the recoverability of the suspension ink, because its initial state can be reached after a high strain stress period. The  $G'$  value is higher than  $G''$  when low strain is applied, which indicates a more gel-like behavior of the ink. However, when a high strain is applied the  $G''$  value is significantly higher than  $G'$  and the suspension shows a liquid-like behavior.<sup>[18,26]</sup> This is a desirable property because it enables the ink to flow through the tip but also its fast curing after its deposition on the substrate to achieve high resolution and maintenance of the resulting printed structure. Similar observations regarding the suspension recovery could be also made for the other analyzed suspensions (Figure S4).

For electrical characterization, the specific resistance of the carbon sheets was analyzed with 4-point measurements (Figure 5a).

With the addition of only 5 wt.% or 10 wt.% of CNTs related to the total carbon content the specific sheet resistance of the carbon films could be reduced by 31% or 45%, respectively. However, a higher amount of CNTs leads to a significant increase in the viscosity which hinders the use of the respective suspensions for the printing process and leads to inhomoge-

neous carbon sheets. This is why the overall carbon content needed to be readjusted to obtain a suitable printability. Consequently, this led to an increase in the specific resistance of the carbon sheets visible exemplarily for the samples CNT10 and CNT10d (increase of 40% in the resistance) as well as CNT50d and CNT50dd (increase of 79% in the resistance). As an optimum CNT20d is prepared with only a small decrease in the carbon content with still relatively high amount of CNTs. The specific resistance of the respective carbon sheet is with 2.34 mΩm similar to the CNT10 sample.

All carbon powders obtained from the different suspensions were analyzed with N<sub>2</sub>-physisorption measurements to evaluate the effect of different CNT content on the resulting specific surface area of the printed electrodes (Figure 5b and c). As expected, the resulting surface area drastically decreases with the addition of EC because non-porous EC increases the total mass of the material while not contributing to a higher surface area. The addition of CNTs further decreases the total surface area of the carbon mixture. With the addition of 10 wt.%, 20 wt.% to 50 wt.% of CNTs the surface area decreases from 667 m<sup>2</sup> g<sup>-1</sup> to 412 m<sup>2</sup> g<sup>-1</sup>, 373 and 303 m<sup>2</sup> g<sup>-1</sup>, respectively.

After the successful printing process of the suspension the respective printed electrodes were analyzed with SEM to evaluate the electrode morphology (Figures 5d–f, S4). With the used suspension synthesis method, the CNTs could be finely distributed over the AC particles for all samples leading to a network-like arrangement of both carbon materials (Figure S5). For the CNT20d and CNT50d electrodes mainly all AC particles are included into this CNT network even on the edge of the printed electrode forming a dense and stable electrode

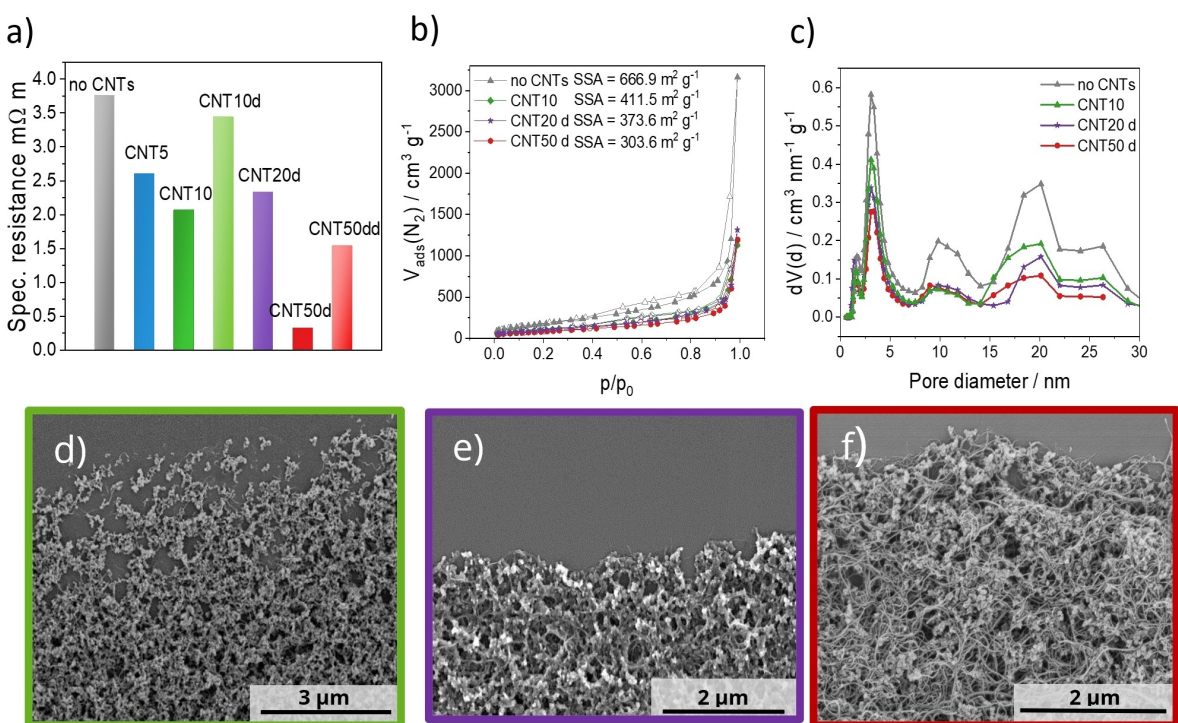


**Figure 5.** a) Specific sheet resistances of the carbon thin films with different CNT amount, b) N<sub>2</sub>-physisorption isotherms at 77 K and c) pore size distribution of the different AC–CNT–EC powder, SEM images of the electrode edges for d) CNT10, e) CNT20d and f) CNT50d.

morphology. For the CNT10 sample, however, the ratio of AC to CNT is not enough to include all AC particles leading to loosely bound AC particle agglomerates or even partly detached from the main electrode area which is especially visible at the electrode edges (Figure 5d–f).

In the next step, the electrochemical performance of the MSCs for the samples CNT10, CNT20d and CNT50d was analyzed and compared to the ones without CNTs using 0.1 M and 1 M H<sub>2</sub>SO<sub>4</sub> as well as a PVA/H<sub>2</sub>SO<sub>4</sub> based gel as electrolyte to form quasi-solid state MSCs.

Among all MSCs the best areal and volumetric capacitances could be achieved with the CNT10 electrodes over the whole scan rate window (13.41 mF cm<sup>-2</sup> and 35.10 F cm<sup>-3</sup> for 5 mV s<sup>-1</sup>) (Figures 6 and S6). Using sulfuric acid in high and low concentrations instead of the gel electrolyte led to similar capacitances (13.23 mF cm<sup>-2</sup> (0.1 M H<sub>2</sub>SO<sub>4</sub>), 14.51 mF cm<sup>-2</sup> (1 M H<sub>2</sub>SO<sub>4</sub>) each at 5 mV s<sup>-1</sup>) at low and high scan rates (Figure S7). This indicates that 0.1 M H<sub>2</sub>SO<sub>4</sub> already provides enough ions for a complete and fast double layer formation.

By changing the electrolyte system, the ESR could be slightly decreased from 2.2 kΩ (gel) to 2.0 kΩ (0.1 M H<sub>2</sub>SO<sub>4</sub>) and 1.8 kΩ (1 M H<sub>2</sub>SO<sub>4</sub>) probably due to a slightly higher proton mobility and concentration in the aqueous electrolyte. To evaluate the charge discharge rate of the different devices the relaxation time constant  $\tau_0$  is calculated (minimum time to discharge a device with an efficiency of 50%, calculation (in supportings)). Smaller  $\tau_0$  values indicate a higher rate capability.<sup>[44–47]</sup> A high proton concentration (1 M H<sub>2</sub>SO<sub>4</sub>) leads to an increase in  $\tau_0$  probably caused by a higher ion congestion in the pore system, which counteracts an unhindered desorption and diffusion process. In comparison to 0.1 M H<sub>2</sub>SO<sub>4</sub>,  $\tau_0$  in the gel electrolyte is also slightly increased probably due to a lower ion mobility of the protons in the gel matrix hindering a fast discharging. The as described trend in the achievable capacitances, ESR and  $\tau_0$  are coherent with the observations made for the other MSCs (no CNTs, CNT20d and CNT50d) (Figure S7, Table 1).

In contrast to the MSC without CNT, the addition of only 10 wt.% CNTs already significantly lowered the ESR and diffusion resistances of the system. Furthermore, the impedance spectra measured before, after cycling and after all measured CVs are very similar over the whole measuring time which indicates a significantly improvement of the system stability, particularly the electrode stability (Figure 6c). Due to the discussed improvements, significantly higher capacitances could be achieved especially for high scan rates even though

the specific surface area of the AC-CNT material is decreased (Figure S6). The above-mentioned observations underline the importance of electrode conductivity and stability against electrode swelling effects next to high surface area of the electrode material to achieve a high capacitance.<sup>[48]</sup>

By further increasing the CNT content to 50 wt.% the ESR of the MSC could be again further decreased down to 1.0 kΩ for the aqueous electrolyte. Additionally, the capacitance decay from low to high scan rates could be decreased especially when using the aqueous electrolyte (for CNT10 48%, for CNT50d 68% capacitance retention, respectively). Slightly lower capacitances could be achieved for the gel electrolyte probably due to a decreased ion accessibility into the dense AC-CNT carbon network which is especially pronounced in gel electrolyte systems where the ion mobility is already more limited than in liquid electrolytes. The overall achievable capacitance for CNT50d, however, is significantly decreased due to the above discussed lower surface area of the electrode material. Accordingly, only about the half of the capacitance of CNT10 at 5 mV s<sup>-1</sup> could be reached.

To achieve capacitances (high surface area, high carbon content) as high as possible while still ensuring a high electrode conductivity and stability, as well as a suitable printability of the suspension, an optimal CNT content of 20 wt.% is chosen. Here, the respective MSC shows a high areal capacitance ranging from 9.91 mF cm<sup>-2</sup> (1 M H<sub>2</sub>SO<sub>4</sub>) and 8.15 mF cm<sup>-2</sup> (gel) while still a high ESR of up to 1.5 kΩ and low  $\tau_0$  of down to 10.8 s could be achieved similar to CNT50d. Also, the low capacitance decay from low to high scan rates is comparable to the CNT50d MSC (65% capacitance retention). For the CNT20d MSC a maximal device capacitance of 3.15 mF cm<sup>-2</sup> at 5 mV s<sup>-1</sup> (gel) could be reached. The achieved capacitances are therefore in or above the range of capacitances of similar 3D-printed state-of-the-art MSCs from literature (Table S1).

To evaluate the cycle stability of the optimized MSC, the system was cycled over 10.000 cycles using gel and 0.1 M H<sub>2</sub>SO<sub>4</sub> respectively. For both systems the MSCs show a remarkable cycling stability with a capacitance retention of only 94.8% (0.1 M H<sub>2</sub>SO<sub>4</sub>) and 104% (gel) after 10.000 cycles (Figure 7). Furthermore, also a 60° bended solid-state MSC was analyzed to evaluate the stability of the system when mechanically stressed. Here, the MSC also showed a high mechanical stability against bending over 10.000 cycles with a high capacitance retention of 93%. Depending on the used electrolytes the CNT20d MSCs showed energy densities up to 1.00–0.70 mWh cm<sup>-3</sup> and power densities up to 0.08 W cm<sup>-3</sup>. There-

**Table 1.** Areal and volumetric capacitances, ESR and relaxation time for the suspensions with different CNT content.

Sample	Areal capacitance at 5 mV s <sup>-1</sup> [mF cm <sup>-2</sup> ] <sup>[a]</sup>	Vol. capacitance at 5 mV s <sup>-1</sup> [F cm <sup>-3</sup> ] <sup>[a]</sup>	ESR [kΩ] <sup>[a]</sup>	Relaxation time constant $\tau_0$ [s] <sup>[a]</sup>
No CNTs	7.71/3.74/5.56	39.04/20.34/28.69	12.0/4.8/6.0	-/32.9/-
CNT10	13.41/13.23/14.51	54.62/53.90/59.13	2.2/2.0/1.8	30.7/25.0/33.0
CNT20d	8.15/7.82/9.91	35.09/33.68/42.68	2.0/1.5/1.5	18.9/10.8/18.3
CNT50d	6.05/6.37/7.53	22.42/23.60/27.91	3.5/1.0/0.9	24.4/10.0/10.8

[a] Capacitances, ESR and relaxation time constant for different electrolyte systems: PVA + H<sub>2</sub>SO<sub>4</sub> gel/0.1 M H<sub>2</sub>SO<sub>4</sub>/1 M H<sub>2</sub>SO<sub>4</sub>.

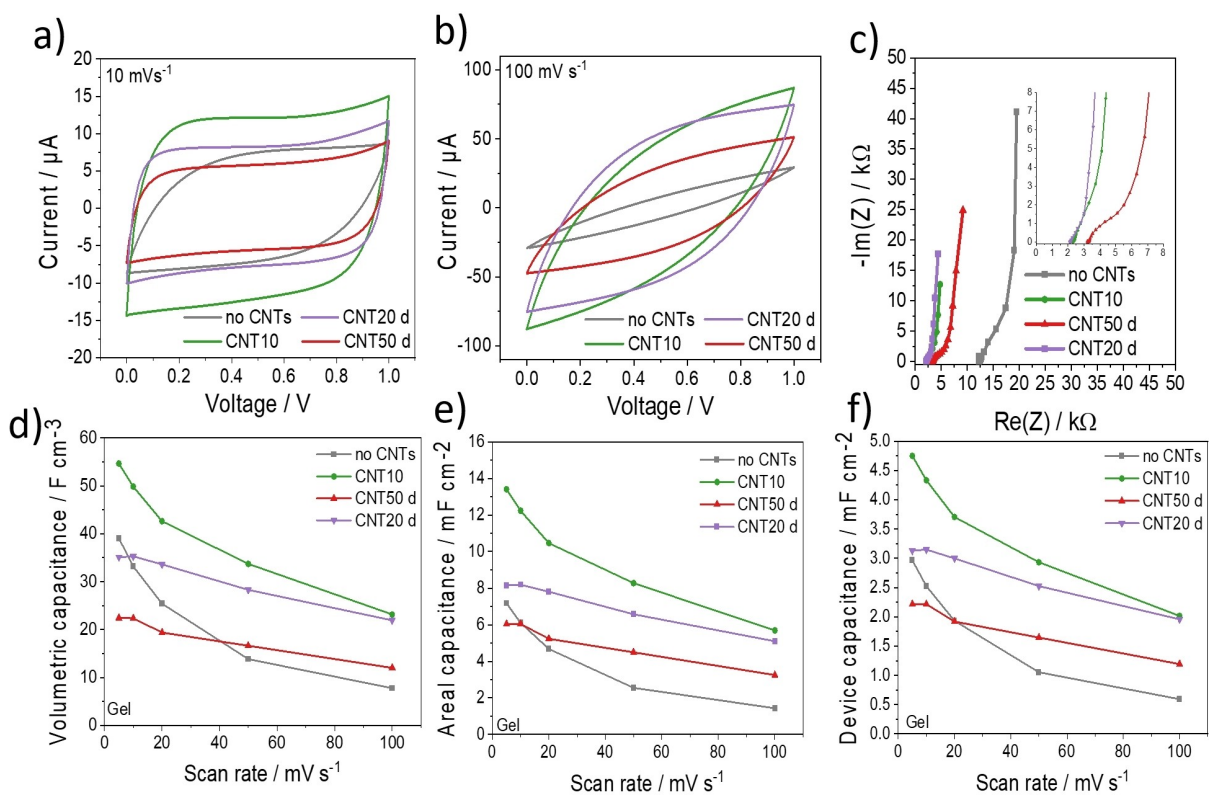


**Figure 6.** CV curves at a)  $10 \text{ mV s}^{-1}$  and b)  $100 \text{ mV s}^{-1}$ , c) impedance spectra, d) volumetric, e) areal and f) device capacitance of the MSCs with different CNT content ( $\text{H}_2\text{SO}_4/\text{PVA}$  as electrolyte).

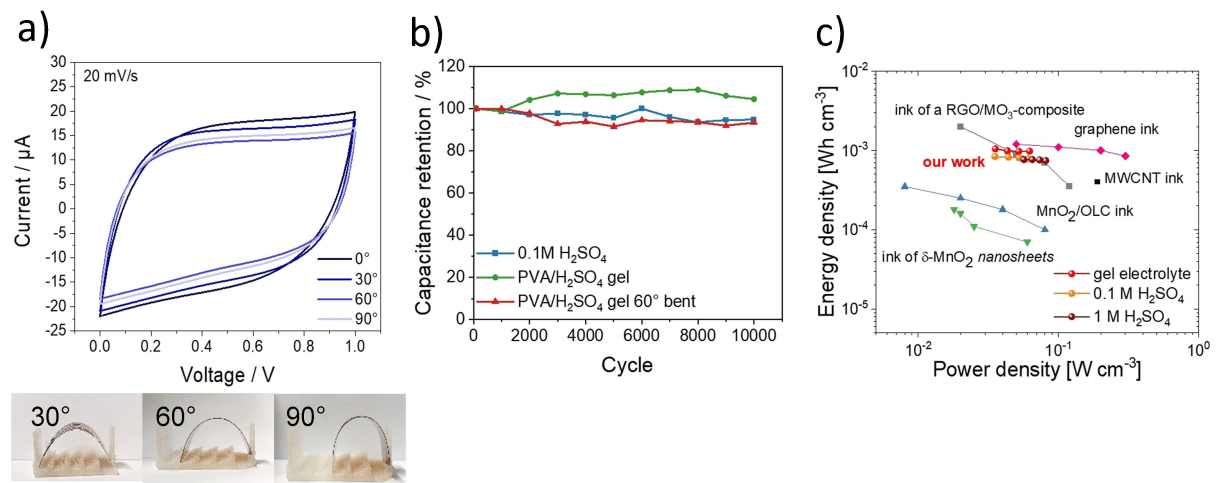


**Figure 7.** CV curve of the CNT20d MSC for different bending angles at  $20 \text{ mV s}^{-1}$  using the gel electrolyte (a), GCD cycling stability over 10,000 cycles (38.9  $\mu\text{A cm}^{-2}$  discharge current) for MSCs using the gel electrolyte (bent and without deformation) and  $0.1 \text{ M H}_2\text{SO}_4$  (b), Ragone plot (c) with different electrolytes using CNT20d MSCs with different electrolytes.

fore, the MSCs exhibit energy and power densities similar to comparable printed MSCs.<sup>[49–53]</sup>

## Conclusions

Herein, we demonstrated the fabrication of a sustainable carbon suspension highly suitable for 3D extrusion printing of

interdigital micro-supercapacitors. The carbon ink contains a mesoporous carbon material with high surface area and is dispersed in a high concentration in cyrene using ethylcellulose as a binder. The 3D extrusion printing of this ink is an environmentally friendly, low cost, fast and versatile method to fabricate flexible MSCs with high-resolution patterned structures. By varying systematically the amount of the ink components, the influence of binder and carbon content on the

overall electrochemical performance and printability was examined. After optimizing the amount of CNTs added to the ink, the resulting MSC show high electronic conductivity with sheet resistances between 3.7 and 0.3 mΩ m, high areal capacitances of up to 13.41 mF cm<sup>-2</sup> and excellent cycle stability over 10.000 cycles, even when bended. The MSCs operate with various electrolytes and prove versatile.

The 3D extrusion printing technique is a powerful tool to design different electrode architectures with dissimilar materials even in complex geometries. Based on the deposition of such non-toxic carbon ink formulations on flexible substrates as demonstrated in this work, printed MSCs may find promising applications in wearable, flexible electronics in future.

## Experimental Section

### Synthesis of carbon suspensions without CNTs

In an appropriate approach 0.19 g Ketjenblack EC600JD (AkzoNobel) and different amounts of ethylcellulose (Sigma Aldrich, viscosity 10 cP) (see Table 2) are finely grinded and added into a mixture of 25.5 mL (0.335 mol) Isopropanol (Sigma Aldrich, 99.99%) and 4.5 mL (0.044 mol) Cyrene (Sigma Aldrich). Afterwards, the mixture was subjected to ultrasonication using an ultrasonication finger (*Labsonic P, Satorius*) for 30 min with cooling in the ice bath. The isopropanol of the resulting suspension was removed in the rotary evaporator at 60 °C bath temperature and 130 mbar so that the carbon content could be significantly increased from 0.74 wt.% to 3.37 wt.% while still obtaining a homogenous stable suspension.

### Synthesis of the carbon suspensions with CNTs

For the suspensions with CNTs different amounts of Ketjenblack were mixed with a fixed amount of EC (80% related to the total carbon content) and different amounts of multiwalled CNTx (Sigma Aldrich, length: 4 μm; inner and outer diameter: 4.5 and 10 nm) while x describes the percentage of the mass ratio of CNTs to the total carbon content), were added. Because the addition of CNTs significantly increases the resultant viscosity of the suspension, the overall carbon content needed to be decreased stepwise to obtain a suitable printability (marked with "d" in the sample name, see Table 3). All further suspension processing steps are kept like described in the synthesis of carbon suspensions without CNTs.

Rheological properties of the inks were analyzed using a *HAAKE Rheostress 1* rheometer from *Thermo Fisher* equipped with a 60 mm double cone geometry in a 1° angle (gap thickness: 52 μm and measurement volume: 2.7 mL, temperature: 25 °C) at shear rate of 1–1000 s<sup>-1</sup>). Next to viscosity determination (measured in rotation mode) also low (0.2 Pa) and high (10 Pa) shear stress were applied repetitively to the inks over four cycles and the respective responses were traced (measuring in oscillation mode). Here, always the second, third and fourth cycle was plotted.

### Extrusion printing of the micro-supercapacitor (MSC) structures

The MSC structures were fabricated using a 3D printer (Bioscaffolder 3.2, GeSim mbH) equipped with an extrusion module. The dimensions of the structures are specified in Figure 3(a). The carbon ink was extruded through a nozzle (160 μm inner diameter) and deposited onto a Kapton film (500 μm thickness). Depending on the viscosity of the ink, air pressures between 10–30 kPa were used with a tip moving speed between 10–15 mm s<sup>-1</sup> for a successful printing with high resolution. After printing, the structures were dried in an oven at 100 °C for at least 1 h in air and further treated at 300 °C in a tube furnace under argon atmosphere.

### Preparation of interdigital MSCs and thin-film EDLCs

The printed structures were contacted with silver conducting paste (*Ferro GmbH*) on the contact pads. Furthermore, a 10×5 mm area around the electrode was surrounded by Kapton foil to define a specific reservoir for the gel electrolyte. When using a gel electrolyte 20 μL of polyvinylalcohol PVA/H<sub>2</sub>SO<sub>4</sub> hydrogel was applied. When sulfuric acid was used, the electrode area of the structure was immersed in a 5 mL reservoir of sulfuric acid.

The thin-film EDLCs were fabricated by drop-casting 4 μL of the carbon suspension on two titanium current collectors (12 mm in diameter) and dried at 50 °C in a drying oven. Afterwards, the electrodes are activated for 12 h at 45 °C at 450 mbar in a vacuum oven. A PVA/H<sub>2</sub>SO<sub>4</sub> hydrogel was applied on the electrode surface and dried at 35 °C. The electrodes were assembled in a Swagelok setup using a polypropylene separator (25 μm thickness, 64 nm pore diameter, *Celgard*).

### Preparation of the gel electrolyte

For the synthesis of solid-state PVA/H<sub>2</sub>SO<sub>4</sub> hydrogel electrolyte 0.5 g (11.35 mmol) of PVA (>98% Merck, molecular weight: 145.000 g mol<sup>-1</sup>) was fully dissolved in 7 mL deionized water and stirred at 90 °C. Afterwards, 0.5 g (5.10 mmol) sulfuric acid (95%, VWR) were added dropwise to the solution under vigorous stirring. The clear electrolyte solution was used for MSCs and thin-film EDLCs.

**Table 2.** Sample composition for the suspensions with different EC content (without CNTs).

sample	Amount of EC [mg]	Mass concentration of EC [wt.%]	Ratio of EC to the total carbon amount [%]
AC-1	55	0.95	29
AC-2	70	1.12	37
AC-3	100	1.69	53
AC-4	151	2.50	80

**Table 3.** Sample composition for the suspensions with different amounts of CNTs.

sample	Amount of CNTs [mg]	Amount of EC [mg]	Amount of total carbon (AC + CNTs) [mg]
No CNTs = AC-4	-	151	190
CNT5	10	151	190
CNT10	20	151	190
CNT10d	14	112	140
CNT20d	34	136	170
CNT50d	70	112	140
CNT50dd	50	80	100

## Fabrication and characterization of compact carbon thin films and carbon powder

Carbon thin films were prepared by spin coating (*Spin 150, ATP GmbH*) 80 µl of the carbon inks on a glass substrate (*Corning 1737, DELTA Technologies*) (25 mm×25 mm×1.1 mm). In order to obtain homogenous thin films, the substrates were pretreated in a piranha solution (1 part 30% H<sub>2</sub>O<sub>2</sub> solution, 3 part conc. H<sub>2</sub>SO<sub>4</sub>) for at least 30 min and cleaned with water and ethanol afterwards. The rotation speed for the spin coating process was adjusted to 2000 min<sup>-1</sup> for 30 s. The films were dried at 100 °C under air or treated at 200 °C or 300 °C in a tube furnace under argon atmosphere. The surface resistances of the carbon thin films were measured using a four-point measurement device (2401 *Source Meter, Keithley*) at room temperature. The thicknesses of the films and structures were determined with atomic force microscopy (AFM) measurements (*Dimension D 3100, Digital Instruments*). The morphology of the films and structures were characterized by Scanning Electron Microscopy (SEM) on a *DSM-982 Gemini* from Zeiss using a voltage of 1–2 keV. The high-resolution transmission electron microscopy (HR-TEM) images were taken with a *JEOL Jem F-200C* – transmission electron microscope equipped with a *Gatan OneView* – in-situ 4 K camera at an acceleration voltage of 200 kV.

To obtain the respective carbon powders, the carbon thin films were scratched off and grinded to a fine powder. The surface area and pore size distribution of the carbon powder was determined via N<sub>2</sub>-physisorption measurements (77 K) using a *Quantachrome* instrument (Quadasorb). Before the measurement, the powders were activated in vacuum at 150 °C for 24 h. The specific surface areas were calculated based on multi-point Brunauer–Emmett–Teller (BET) method in the range of  $p/p_0 = 0.05\text{--}0.2$ . The respective pore size distributions were determined using the Quenched-Solid-Density-Functional-Theory (QSDFT) calculation method for carbon (slit pores).

## Electrochemical characterization

The sandwich-like EDLCs and in-plane MSCs were electrochemically analyzed with a *VMP3* potentiostat from *BioLogic Science Instruments* in a two-electrode setup. Cyclic voltammetry measurements were conducted in a potential range of 0 to +1 V using scan rates between 5–100 mVs<sup>-1</sup>. Electrochemical Impedance Spectroscopy (EIS) measurements were carried out in a frequency range from 5 mHz to 100 kHz at open circuit potential with a voltage amplitude of 10 mV. Galvanostatic charging and discharging (GCD) measurements were executed in the range of 0–1 V using charging and discharging rates from 22.2–38.9 µAcm<sup>-2</sup> for MSCs and 25.5–63.7 µAcm<sup>-2</sup> for thin-film EDLCs.

## Supporting Information

Supporting Information is available from the Wiley Online Library or from the author. The authors have cited additional references within the Supporting Information.<sup>[14,19,46,49,53,54]</sup>

## Acknowledgements

We gratefully thank the European Research Council (ERC) under the European Union's Horizon Europe research and innovation program (grant agreement No. 101054940) for financial support. We thank Leonid Shupletsov for conducting the HRTEM

measurements and Ankita De for the SEM images. The authors also acknowledge the use of the facilities in the Dresden Center for Nanoanalysis (DCN) at the Technische Universität Dresden. Open Access funding enabled and organized by Projekt DEAL.

## Conflict of Interests

The authors declare no conflict of interest.

## Data Availability Statement

The data that support the findings of this study are available from the corresponding author upon reasonable request.

**Keywords:** 3D extrusion printing • flexible micro-supercapacitor • sustainable carbon ink • porous carbon

- [1] Y. Z. Zhang, Y. Wang, T. Cheng, L. Q. Yao, X. Li, W. Y. Lai, W. Huang, *Chem. Soc. Rev.* **2019**, *48*, 3229–3264.
- [2] S. Gong, W. Cheng, *Adv. Energy Mater.* **2017**, *7*, 1700648.
- [3] H. Park, Y. Lee, N. Kim, D. Seo, G. Go, T. Lee, *Adv. Mater.* **2020**, *32*, 1903558.
- [4] G. Bruno, G. Canavese, X. Liu, C. S. Filgueira, A. Sacco, D. Demarchi, M. Ferrari, A. Grattoni, *Nanoscale* **2016**, *8*, 18718–18725.
- [5] G. Wu, P. Tan, X. Wu, L. Peng, H. Cheng, C. F. Wang, W. Chen, Z. Yu, S. Chen, *Adv. Funct. Mater.* **2017**, *27*, 1–11.
- [6] D. Pech, M. Brunet, H. Durou, P. Huang, V. Mochalin, Y. Gogotsi, P. L. Taberna, P. Simon, *Nat. Nanotechnol.* **2010**, *5*, 651–654.
- [7] E. Frackowiak, *Phys. Chem. Chem. Phys.* **2007**, *9*, 1774.
- [8] E. Frackowiak, F. Béguin, *Carbon* **2001**, *39*, 937–950.
- [9] M. Beidaghi, Y. Gogotsi, *Energy Environ. Sci.* **2014**, *7*, 867–884.
- [10] J. W. Boley, E. L. White, G. T. C. Chiu, R. K. Kramer, *Adv. Funct. Mater.* **2014**, *24*, 3501–3507.
- [11] D. P. Parekh, C. Ladd, L. Panich, K. Moussa, M. D. Dickey, *Lab Chip* **2016**, *16*, 1812–1820.
- [12] B. Zhang, S. H. Chung, S. Barker, D. Craig, R. J. Narayan, J. Huang, *Prog. Nat. Sci. Mater. Int.* **2021**, *31*, 180–191.
- [13] M. Zarek, M. Layani, I. Cooperstein, E. Sachyani, D. Cohn, S. Magdassi, *Adv. Mater.* **2016**, *28*, 4449–4454.
- [14] W. Yu, H. Zhou, B. Q. Li, S. Ding, *ACS Appl. Mater. Interfaces* **2017**, *9*, 4597–4604.
- [15] Z. Wang, Q. Zhang, S. Long, Y. Luo, P. Yu, Z. Tan, J. Bai, B. Qu, Y. Yang, J. Shi, H. Zhou, Z. Y. Xiao, W. Hong, H. Bai, *ACS Appl. Mater. Interfaces* **2018**, *10*, 10437–10444.
- [16] S. H. Huang, P. Liu, A. Mokasdar, L. Hou, *Int. J. Adv. Manuf. Technol.* **2013**, *67*, 1191–1203.
- [17] E. Ordoñez, J. M. Gallego, H. A. Colorado, *Appl. Clay Sci.* **2019**, *182*, 105285.
- [18] H. Li, J. Liang, *Adv. Mater.* **2020**, *32*, 1–19.
- [19] Y. Bräuniger, S. Lochmann, J. Grothe, M. Hantusch, S. Kaskel, *ACS Appl. Energ. Mater.* **2021**, *4*, 1560–1567.
- [20] T. D. Ngo, A. Kashani, G. Imbalzano, K. T. Q. Nguyen, D. Hui, *Composites Part B* **2018**, *143*, 172–196.
- [21] M. Schouten, G. Wolterink, A. Dijkshoorn, D. Kosmas, S. Stramigoli, G. Krijnen, *IEEE Sens. J.* **2021**, *21*, 12900–12912.
- [22] M. Abas, Q. Salman, A. M. Khan, K. Rahman, *J. Brazilian Soc. Mech. Sci. Eng.* **2019**, *41*, 1–11.
- [23] K. Hassan, T. T. Tung, N. Stanley, P. L. Yap, F. Farivar, H. Rastin, M. J. Nine, D. Losic, *Nanoscale* **2021**, *13*, 5356–5368.
- [24] S. Chandrasekaran, B. Yao, T. Liu, W. Xiao, Y. Song, F. Qian, C. Zhu, E. B. Duoss, C. M. Spadaccini, Y. Li, M. A. Worsley, *Mater. Horiz.* **2018**, *5*, 1166–1175.
- [25] K. Sun, T. S. Wei, B. Y. Ahn, J. Y. Seo, S. J. Dillon, J. A. Lewis, *Adv. Mater.* **2013**, *25*, 4539–4543.
- [26] K. Fu, Y. Yao, J. Dai, L. Hu, *Adv. Mater.* **2017**, *29*, 1603486.
- [27] K. Shen, J. Ding, S. Yang, *Adv. Energy Mater.* **2018**, *8*, 1–7.

- [28] K. Hassan, M. J. Nine, T. T. Tung, N. Stanley, P. L. Yap, H. Rastin, L. Yu, D. Lasic, *Nanoscale* **2020**, *12*, 19007–19042.
- [29] X. Yun, B. Lu, Z. Xiong, B. Jia, B. Tang, H. Mao, T. Zhang, X. Wang, *RSC Adv.* **2019**, *9*, 29384–29395.
- [30] H. A. Loh, A. R. Graves, C. D. Stinespring, K. A. Sierros, *ACS Appl. Nano Mater.* **2019**, *2*, 4104–4112.
- [31] X. Wu, F. Mu, Z. Lin, *Mater. Today* **2021**, *11*, 100157.
- [32] T. S. Tran, N. K. Dutta, N. R. Choudhury, *Adv. Colloid Interface Sci.* **2018**, *261*, 41–61.
- [33] M. Santhiago, C. C. Corrêa, J. S. Bernardes, M. P. Pereira, L. J. M. Oliveira, M. Strauss, C. C. B. Bufon, *ACS Appl. Mater. Interfaces* **2017**, *9*, 24365–24372.
- [34] D. Pech, M. Brunet, P. L. Taberna, P. Simon, N. Fabre, F. Mesnilgrente, V. Conédéra, H. Durou, *J. Power Sources* **2010**, *195*, 1266–1269.
- [35] Y. Zheng, X. Huang, J. Chen, K. Wu, J. Wang, X. Zhang, *Materials (Basel)* **2021**, *14*, 3911.
- [36] H.-J. Choi, M. S. Kim, D. Ahn, S. Y. Yeo, S. Lee, *Sci. Rep.* **2019**, *9*, 6338.
- [37] T. Sathies, P. Senthil, C. Parakash, *Mater. Res. Express* **2019**, *6*, 115349.
- [38] N. Vidakis, M. Petousis, E. Veliakis, N. Mountakis, S. Grammatikos, L. Tzounis, *Compos. Struct.* **2023**, *311*, 116788.
- [39] R. Neffati, J. M. C. Brokken-Zijp, *Mater. Chem. Phys.* **2021**, *260*, 124177.
- [40] Y. Yoo, J. Park, M.-S. Kim, W. Kim, *J. Power Sources* **2017**, *360*, 383–390.
- [41] R. Bajpai, S. Roy, N. Kulshrestha, J. Rafiee, N. Koratkar, D. S. Misra, *Nanoscale* **2012**, *4*, 926–930.
- [42] M. Shrestha, I. Amatya, K. Wang, B. Zheng, Z. Gu, Q. H. Fan, *J. Energy Storage* **2017**, *13*, 206–210.
- [43] Y. Rho, K. T. Kang, D. Lee, *Nanoscale* **2016**, *8*, 8976–8985.
- [44] S. Zhang, N. Pan, *Adv. Energy Mater.* **2015**, *5*, 1401401.
- [45] P. L. Taberna, P. Simon, J. F. Fauvarque, *J. Electrochem. Soc.* **2003**, *150*, A292.
- [46] A. Oz, S. Hershkovitz, N. Belman, E. Tal-Gutelmacher, Y. Tsur, *Solid State Ionics* **2016**, *288*, 311–314.
- [47] J. Zhang, X. S. Zhao, *ChemSusChem* **2012**, *5*, 818–841.
- [48] C. Gellrich, S. Lochmann, T. Otto, J. Grothe, S. Kaskel, *Mater Adv* **2021**, *2*, 6380–6387.
- [49] J. Li, S. Sollami Delekta, P. Zhang, S. Yang, M. R. Lohe, X. Zhuang, X. Feng, M. Östling, *ACS Nano* **2017**, *11*, 8249–8256.
- [50] B. Li, N. Hu, Y. Su, Z. Yang, F. Shao, G. Li, C. Zhang, Y. Zhang, *ACS Appl. Mater. Interfaces* **2019**, *11*, 46044–46053.
- [51] Y. Wang, Y. Shi, C. X. Zhao, J. I. Wong, X. W. Sun, H. Y. Yang, *Nanotechnology* **2014**, *25*, 094010.
- [52] Y. Wang, Y. Z. Zhang, D. Dubbink, J. E. ten Elshof, *Nano Energy* **2018**, *49*, 481–488.
- [53] S. K. Kim, H. J. Koo, A. Lee, P. V. Braun, *Adv. Mater.* **2014**, *26*, 5108–5112.
- [54] A. Sajedi-Moghadam, M. Gholami, N. Naseri, *ACS Appl. Mater. Interfaces* **2023**, *15*, 3894–3903.

---

Manuscript received: October 11, 2023

Revised manuscript received: November 6, 2023

Accepted manuscript online: November 13, 2023

Version of record online: December 7, 2023

---